Journal of Luminescence 170 (2016) 431–443

Contents lists available at ScienceDirect

Journal of Luminescence

journal homepage: www.elsevier.com/locate/jlumin

Near infrared emission and multicolor tunability of enhanced upconversion emission from Er^{3+}–Yb^{3+} co-doped Nb_2O_5 nanocrystals embedded in silica-based nanocomposite and planar waveguides for photonics

Felipe Thomaz Aquino [a], Jefferson Luis Ferrari [a,b], Lauro June Queiroz Maia [c], Sidney José Lima Ribeiro [d], Alban Ferrier [e,f], Philippe Goldner [e], Rogéria Rocha Gonçalves [a,*]

[a] Departamento de Química, Faculdade de Filosofia, Ciências e Letras de Ribeirão Preto, Universidade de São Paulo. Av. Bandeirantes, 3900, CEP 14040-901 Ribeirão Preto, SP, Brazil
[b] Grupo de Pesquisa em Química de Materiais – (GPQM), Departamento de Ciências Naturais, Universidade Federal de São João Del Rei, Campus Dom Bosco, Praça Dom Helvécio, 74, 36301-160 São João Del Rei, MG, Brazil
[c] Grupo Física de Materiais, Instituto de Física, Universidade Federal de Goiás, Campus II, C.P. 131, CEP 74001-970, Goiânia, GO, Brazil
[d] Institute of Chemistry- São Paulo State University- UNESP, Araraquara, SP 14800-900, Brazil
[e] PSL Research University, Chimie ParisTech - CNRS, Institut de Recherche de Chimie Paris, 75005 Paris, France
[f] Sorbonne Universités, UPMC Univ Paris 06, 75005 Paris, France

ARTICLE INFO

Article history:
Received 18 December 2014
Received in revised form
22 April 2015
Accepted 25 August 2015
Available online 14 September 2015

Keywords:
Upconversion
Sol–gel
Broadband NIR emission
Nb_2O_5

ABSTRACT

This work reports on the Yb^{3+} ion addition effect on the near infrared emission and infrared-to-visible up conversion from planar waveguides based on Er^{3+}–Yb^{3+} co-doped Nb_2O_5 nanocrystals embedded in SiO_2-based nanocomposite prepared by a sol–gel process with controlled crystallization in situ. Planar waveguides and xerogels containing Si/Nb molar ratio of 90:10 up to 50:50 were prepared. Spherical-like orthorhombic or monoclinic Nb_2O_5 nanocrystals were grown in the amorphous SiO_2-based host depending on the niobium content and annealing temperature, resulting in transparent glass ceramics. Crystallization process was intensely affected by rare earth content increase. Enhancement and broadening of the NIR emission has been achieved depending on the rare earth content, niobium content and annealing temperature. Effective $Yb^{3+} \rightarrow Er^{3+}$ energy transfer and a high-intensity broad band emission in the near infrared region assigned to the Er^{3+} ions $^4I_{13/2} \rightarrow {}^4I_{15/2}$ transition, and longer $^4I_{13/2}$ lifetimes were observed for samples containing orthorhombic Nb_2O_5 nanocrystals. Intense green and red emissions were registered for all Er^{3+}–Yb^{3+} co-doped waveguides under 980 nm excitation, assigned to $^2H_{11/2} \rightarrow {}^4I_{15/2}$ (525 nm), $^4S_{3/2} \rightarrow {}^4I_{15/2}$ (545nm) and $^4F_{9/2} \rightarrow {}^4I_{15/2}$ (670 nm) transitions, respectively. Different relative green and red intensities emissions were observed, depending upon niobium oxide content and the laser power. Upconversion dynamics were determined by the photons number, evidencing that ESA or ETU mechanisms are probably occurring. The 1931 CIE chromaticity diagrams indicated interesting color tunability based on the waveguides composition and pump power. The nanocomposite waveguides are promising materials for photonic applications as optical amplifiers and WDM devices operating in the S, C, and L telecommunication bands; and as upconverter materials for visible upconversion lasers, biomedical applications, energy conversion for solar cells and others.

1. Introduction

Concerning technological applications in photonics and biophotonics, lanthanide doped compounds represent today one of the most important class of materials which can be used in a huge number of areas as telecommunication, energy, medical and biomedical, environmental, optics, applications to quantum information processing, among others [1–3]. Considering the lanthanide ions, Er^{3+} ions are particularly interesting as near infrared (NIR) emitter (around 1550 nm) [2,4,5], which are applied as main active component in Erbium-Doped Fiber Amplifiers (EDFAs) and Erbium-Doped Planar Waveguide Amplifiers (EDPWAs) for telecom. In the case of EDPWAs there is nowadays a considerable effort in research of new materials, compositions and methods for

* Corresponding author. Tel.: +55 16 36024851; fax: +55 16 36338151.
E-mail address: rrgoncalves@ffclrp.usp.br (R.R. Gonçalves).

http://dx.doi.org/10.1016/j.jlumin.2015.08.077
0022-2313/

the development of optical devices with broader emission to cover not only the C-telecommunication band but also allow its operation in the S- and L- bands [6].

The sol–gel method has been employed for development of lanthanide doped photonic materials, and, with respect to Er^{3+} doped planar waveguides, SiO_2–M_xO_y binary oxides (M=Ti, Zr, Hf, Ta, and Nb) have been successfully described in literature. SiO_2 has interesting properties concerning chemical durability, transparency at 1.5 μm, in addition to its well established use in photonic applications as optical fibers and amplifiers. Besides, the addition of transition metal oxides in SiO_2 enables control of many properties such as refractive index, mechanical and structural properties. As a consequence, the distribution of lanthanide ions in a confined microenvironment, which exhibits lower phonon energy, higher refractive index, higher solubility of lanthanide ions, gives rise to particular interesting luminescent properties. In this sense, the optical properties and their correlation with structural features of sol–gel SiO_2–TiO_2 [7,8], SiO_2–HfO_2 [9–14], SiO_2–ZrO_2 [15–18], SiO_2–Ta_2O_5 [6,19] and SiO_2–Nb_2O_5 [20,21] have been reported in the last years for NIR applications. In previous papers [20,21], we have described in details the NIR luminescence properties of Er^{3+}-doped SiO_2–Nb_2O_5 nanocomposites and pointed out a broadening of emission even though the Er^{3+} ions are located in Nb_2O_5 nanoparticles. This unique and unusual broadening in a specific glass ceramic material, has been explained owing to the particular complex orthorhombic crystalline structure of the niobium oxide [21]. Regarding lanthanide hosts, Nb_2O_5 has important characteristics, such as transparency over a wide range of wavelengths, low cut off energy ($<900\ cm^{-1}$), high refractive index, and the possibility of incorporating high concentrations of lanthanide ions. Nb_2O_5 has also different polymorphic structures, which can modify the materials properties, like luminescence [22,23]. Moreover, the addition of Nb_2O_5 can reduce the presence of OH groups, which quenches the rare earth luminescence and results in shorter excited state lifetime [24].

With respect to the broadband NIR emission of Er^{3+}-doped materials, most of the results concern tellurite glasses [25,26]. However, it is difficult to obtain low-loss planar waveguides with these materials, especially when a soft chemistry synthetic route is employed. Therefore, obtaining broadband emission in silica-based glass ceramic represents an important advantage.

The addition of Yb^{3+} ions as sensitizers of Er^{3+} has been extensively reported in literature [27]. Yb^{3+} ions have a higher cross-section at 980 nm and their $^2F_{5/2}\rightarrow{}^2F_{7/2}$ transition and the $^4I_{15/2}\rightarrow{}^4I_{11/2}$ transition of Er^{3+} ions are nearly resonant, allowing an efficient energy transfer, which can enhance the NIR luminescence. Moreover, upconversion (UC) processes can take place efficiently. The upconversion phenomena was firstly explained in 1960's [28], and although a huge number of works have been devoted to UC processes [28,29], today many distinct applications such as visible range lasers [30], energy converter for solar cells [31–33], displays [34] and biological markers [35–37], among others are very actively studied. Most of the works investigating UC are related to halide crystals [29], glasses and glass ceramics, particularly oxyfluorides, phosphates, germanates and tellurides bulks and fibers [38–44]. Only a very few investigations are related to films and planar waveguides [45–47]. Planar waveguides with intense UC can be extremely interesting for obtaining a compact laser using low cost diode lasers as a pump source, not to mention its potential as solar concentrators [48]. As far as we know, there are no other literature reports on UC emission on Er^{3+}-doped and/or Er^{3+}/Yb^{3+}co-doped SiO_2–Nb_2O_5 materials. Beside of this, in this work, it was demonstrated the possibility of multicolor tunability based on the waveguides composition and pump power. The luminescence combined with optical properties of the planar waveguides make them potential materials for photonics.

One of the main concerns of this study is related to the effect of the Yb^{3+} addition on structure and its correlation with luminescent properties of Er^{3+} doped SiO_2–Nb_2O_5 nanocomposites and planar waveguides, which are prepared by the sol–gel method. As the luminescence features are strictly dependent on the matter structure, i.e., symmetry occupied by lanthanide (Ln^{3+}) ions, ligand/crystal field, refractive index, host phonon energy, and ion–ion (Ln^{3+}) distance, enhancement and broadening of the NIR emission has been achieved depending on the lanthanide and niobium content and annealing temperature. The structural change caused by lanthanide content increase, through Yb^{3+} addition, and its effect on the NIR luminescence of Er^{3+} are carefully discussed. Multicolor tunability of enhanced UC emission has been evaluated as a function of the laser power source and composition.

2. Experimental procedure

Er^{3+}–Yb^{3+} co-doped $(1-x)$–SiO_2–xNb_2O_5 nanocomposites and waveguides were prepared by the sol–gel method. The starting precursors were Niobium ethoxide (Aldrich – 99.95%) and Tetraethylorthosilicate, TEOS (Merck-98%). $ErCl_3$ and $YbCl_3$ were used as Er^{3+} and Yb^{3+} ions precursors, which were obtained from their respective oxides by dissolution in 0.1 mol L^{-1} HCl aqueous solution, followed by careful drying and addition of anhydrous ethanol, resulting in a stock ethanolic solution. Solutions with a total concentration of Si+Nb equal to 0.448 mol L^{-1} were obtained at Si:Nb molar ratios of 90:10, 80:20, 70:30, 60:40, and 50:50. The Er^{3+} and Yb^{3+} ions concentrations were 0.3 mol% and 1.2 mol% respectively (with respect to the total concentration of Si+Nb).

The Si precursor solution (solution 1) was prepared using TEOS, anhydrous ethanol, and HCl at a 50:1 TEOS/HCl volume ratio. Solution 2, containing the Nb precursor, was prepared from a mixture of niobium ethoxide and 2-ethoxyethanol, at a 10:1 2-ethoxyethanol/niobium ethoxide volume ratio, and Er^{3+} and Yb^{3+} ions were also added. Afterwards, solutions 1 and 2 were mixed and the final solution was kept under stirring at room temperature for 30 min. Lastly, a 0.27 mol L^{-1} HCl aqueous solution was added at room temperature, at a 1:0.007 TEOS/HCl molar ratio. The final solution was filtered through a 0.2 μm Millipore filter and left to stand for 16 hrs. The waveguides were deposited onto silica on silicon substrates (10 μm SiO_2–Si(100) *p*-type) by dip-coating technique, at a dipping rate of 30 mm/min. After each deposited layers, the waveguides were annealed for 60 s at 900 °C, until 50 layers were achieved. The waveguides will be labeled as W1–W5 from now on for Si:Nb molar ratios of 90:10, 80:20, 70:30, 60:40, and 50:50, respectively.

After the waveguides deposition, the solutions were maintained at room temperature for about 60 days, for xerogel formation. The resulting xerogels were then ground to powder and annealed in an electrical furnace at 900, 1000 and 1100 °C for 10 hrs. The $(1-x)SiO_2$–xNb_2O_5 nanocomposites obtained will be labeled as S1–S5 from now on for Si:Nb molar ratios of 90:10, 80:20, 70:30, 60:40, and 50:50, respectively.

The X-ray diffraction (XRD) analyzes were carried out on a Siemens-Bruker D5005-AXS diffractometer, with CuKα radiation, graphite monochromator, $\lambda=1.5418$ Å, at 0.02°/s, in the 5-80° 2θ range. The photoluminescence (PL) spectra in the near infrared region (NIR) were registered on a spectrofluorometer Fluorolog 3-222 (FL3-222) Horiba Jobin Yvon equipped with a cooled Ge detector (77K, liquid N_2), and the excitation source was a 980 nm diode laser with power of 800 mW and 2000 mW for the waveguides. Luminescence NIR decay curves were recorded using a pulsed excitation at 980 nm provided by an OPO pumped by a

tripled Nd:YAG laser (Ekspla) producing 10 ns pulses and by recording the signal with a digital oscilloscope. The upconversion emission spectra were recorded using a 980 nm diode laser for excitation and a spectrometer (AVASpec-1024TEC). Signals were collected using an integrating sphere and optical fiber, and the setup, including the integrating sphere and spectrometer was calibrated with a halogen tungsten lamp (10 W tungsten halogen fan-cooled Avalight-HAL) [32]. All the measurements were performed at room temperature.

3. Results and discussion

3.1. Nanocomposites

3.1.1. Structural properties

The structural study will be presented in detail because it is fundamental to understand the luminescent properties. Even though the structural features, i.e., the Nb_2O_5 crystallization, are very close to those already reported by some of us for the $(1-x)SiO_2$–xNb_2O_5 nanocomposites [20,21], the higher rare earth content with the Yb^{3+} ions addition promotes some crystallization change, which will affect the luminescence. The X-ray diffractograms of all the Er^{3+}/Yb^{3+} co-doped $(1-x)SiO_2$–xNb_2O_5 nanocomposites (S1–S5) annealed at 900, 1000, or 1100 °C are shown in Fig. 1(A)–(C), respectively. A large background between 15° and 40° in 2θ, with two maxima at 23° and 29°, was detected in the diffractogram of sample S1 in Fig. 1A, which corresponds to the amorphous silica-based host (JCPDS Card number 029-0085). In addition, the two maxima overlapping this silica halo at 23° and 29°, indicates initial Nb_2O_5 crystallization. Comparing with the previous paper [21] where no diffraction peaks related to the crystalline Nb_2O_5 were detected for the analogous S1 sample, this represents the first evidence that the amount of rare earth ion participates in the crystallization process and glass ceramic formation. This peak becomes more pronounced with increasing Nb_2O_5 content, as well as a decrease of the background intensity, which can be directly associated with partial crystallization. Finally, for samples S4 and S5, better-defined peaks were observed, which can be attributed to orthorhombic Nb_2O_5, known as the T-phase (JCPDS 01-071-0336) or γ-phase [21,22,49], similar to the one observed on $(1-x)SiO_2$–xNb_2O_5 nanocomposites (doped with lower RE content) [21]. The diffraction peaks of S4 and S5 nanocomposites annealed at 900 °C are comparable to that of pure Nb_2O_5 heated at 600 °C, which crystallizes in the orthorhombic T-phase, as observed before [21].

Fig. 1(B) depicts the XRD diffractograms of samples S1–S5 annealed at 1000 °C. T-phase formation can also be observed, mainly for samples S3–S5, which display higher crystallinity and well defined diffraction peaks. Compared with the S1–S5 samples annealed at 900 °C, there is a decrease in the line width, indicating larger crystallite size upon rising temperature.

For the samples annealed at 1100 °C shown in Fig. 1(C), an Nb_2O_5 crystalline phase transformation could be observed for samples S2 to S5. The peaks can be attributed to monoclinic Nb_2O_5, named M-phase and also known as β-phase (JCPDS 00-019-0862) [21,22,49]. In the previous paper [21], practically complete conversion of the T-phase into M-phase was observed for Er^{3+}-doped nanocomposites. Nevertheless, in the present work, additional intense diffraction peaks compared to the ones of M-phase could be observed, which can be attributed to T-phase, and are marked with an asterisk (*) symbol in Fig. 1(C). The sample S1 remained mainly amorphous, still showing a large background, even for this annealing temperature.

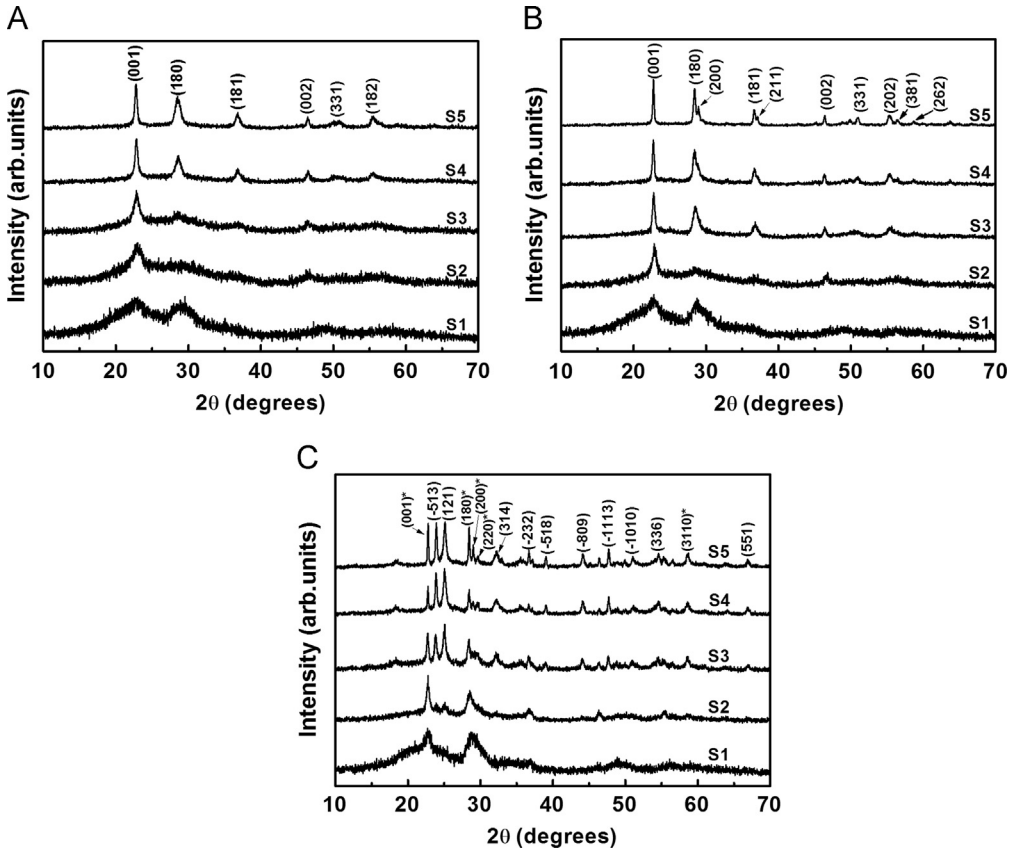

Fig. 1. X-ray diffractograms of 0.3 mol % Er^{3+}/1.2 mol% Yb^{3+} co-doped $(1-x)SiO_2$-xNb_2O_5 nanocomposites (A) S1, S2, S3, S4 and S5 annealed at 900 °C; (B) S1, S2, S3, S4 and S5 annealed at 1000 °C; and (C) S1, S2, S3, S4 and S5 annealed at 1100 °C.

Accordingly, it has been concluded that the higher amount of Ln^{3+} not only favor the T-phase crystallization at lower temperatures (in the case of samples S1 and S2), but also a T-phase stability at higher temperature (1100 °C), occurring only partial phase transformation to the M-phase. This small but significant structural change gives an indication of the Ln^{3+} ions distribution preferably in the niobium oxide host.

3.1.2. NIR photoluminescence spectroscopy

A broad NIR emission was observed for the nanocomposites S2–S5. Luminescence spectra for the nanocomposites annealed at 900, 1000 and 1100 °C are depicted in Fig. 2(A)–(C), respectively. The only exception is the sample S1 that showed a luminescence quenching as a consequence of multiphonon relaxation due to the presence of OH groups.

The maximum peak around 1530 nm observed for all the samples can be assigned to the $^4I_{13/2} \rightarrow {}^4I_{15/2}$ transition of Er^{3+} ions. The inhomogeneous broadening indicates the presence of Er^{3+} ions in different sites of the nanocomposite structures combined with Stark splitting. Analysis of the spectra reveals a clear shape and bandwidth dependence on the niobium content and annealing temperature. The full width at half-maximum (FWHM) values are presented in Table 1. For sample S2, annealed at different temperatures, the FWHM values were similar, in agreement with the XRD analysis, where practically only the orthorhombic crystalline phase is formed (T-phase), even at 1100 °C, presenting very few peaks that can be attributed to M-phase. So, the Er^{3+} ions are occupying sites of the same crystalline structure. For S3 sample, the FWHM values also corroborate with XRD analysis, i.e., at 900 and 1000 °C, the T-phase crystallizes, with higher

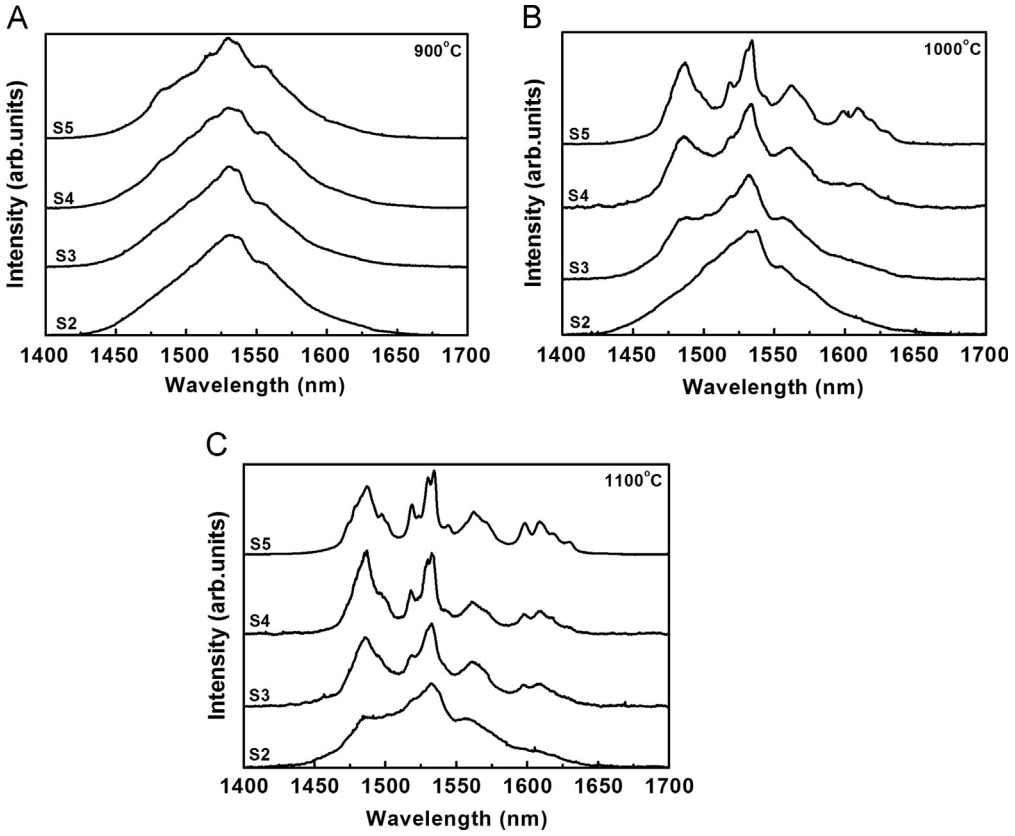

Fig. 2. NIR photoluminescence spectra relative to the $^4I_{13/2} \rightarrow {}^4I_{15/2}$ transition of the Er^{3+} ions of 0.3 mol% Er^{3+}/1.2 mol% Yb^{3+} co-doped (1-*x*)SiO_2-*x*Nb_2O_5 nanocomposites annealed at: (A)900 °C, (B) 1000 °C and (C) 1100 °C for 10 hrs upon excitation at 980 nm.

Table 1
FWHM and $^4I_{13/2}$ excited level lifetime values comparison for Er^{3+}/Yb^{3+} co-doped $(1-x)SiO_2$–xNb_2O_5 nanocomposites S2, S3, S4 and S5 annealed at 900 °C, 1000 °C and 1100 °C.

Samples (°C)	Main emission peak (nm)	FWHM (nm)	$^4I_{13/2}$ excited level lifetime (ms) ($\tau_{1/e}$) ± 0.1 ms	$^4I_{13/2}$excited level lifetime (ms) (2nd order exponential) ± 0.1 ms
S2 – 900	1531	83	3.0	1.4/6.0
S2 – 1000	1532	80	2.6	1.1/5.0
S2 – 1100	1533	86	1.4	0.9/4.9
S3 – 900	1530	76	3.6	1.4/5.4
S3 – 1000	1532	86	2.4	1.2/5.2
S3 – 1100	1533	65	1.1	0.2/3.7
S4 – 900	1530	89	2.6	1.3/4.1
S4 – 1000	1534	89	1.5	1.1/4.2
S4 – 1100	1533	58	0.5	0.3/4.0
S5 – 900	1530	86	2.0	1.0/3.1
S5 – 1000	1534	63	0.4	0.2/3.3
S5 – 1100	1534	59	0.2	0.3/3.1

crystallinity for the latter, and at 1100 °C, an admixture of T- and M-phases occurs. Because of that, the FWHM values are much higher for the samples annealed at 900 and 1000 °C and decrease for 1100 °C. This behavior also can be clearly observed on Fig. 3 (A) where the spectra at 900 and 1000 °C shown similar shape, while a different shape of spectra was observed for 1100 °C. For samples S4 and S5 there was a decrease in the FWHM values even for 1000 °C, which can indicate an admixture of phases being already formed for this annealing temperature, although we did not observe it by XRD analysis.

The behavior observed on the FWHM values indicates that Er^{3+} ions are occupying Nb_2O_5-rich environment with different polymorphs, as it was well described in a previous paper [21]. As reported in the literature, the orthorhombic T-phase presents niobium ions in different pentagonal bipyramids and octahedral symmetry sites, while in the monoclinic phase the metal ions occupy octahedral symmetry sites, in a more ordered crystalline phase. The distribution of Er^{3+} in orthorhombic Nb_2O_5 nanocrystals, with substitutional or interstitial doping host, explains the large FWHM values of about 84 nm observed for the samples containing the respective phase [21]. Accordingly, inhomogeneous broadening reduction for the Er^{3+} emission has been observed when the lanthanide ions are located in monoclinic Nb_2O_5 host [21].

Another contribution to the inhomogeneous broadening is the distribution of Er^{3+} ions bonded to SiO^- terminal groups. In this kind of nanocomposite, the addition of niobium to the silica network can promote rupture, with formation of Si–O–Nb linkage and terminal $Si–O^-$ groups. Also, higher amount of rare earth ions can promote some disruption, and consequently bonds between lanthanide ions and terminal oxygen ($Si–O^-$) can also be established in different microenvironments, contributing to broadening of the emission spectra, which has already been reported for pure SiO_2 [50]. Since the inhomogeneous broadening observed here is very close to those of Er^{3+} in pure Nb_2O_5, this effect can be considered small.

The FWHM values of the present work were higher than those previously obtained in our group in Er^{3+}-doped $(1-x)SiO_2–xNb_2O_5$ nanocomposites, which can be explained by the influence of Yb^{3+} ions on the orthorhombic crystallization and stability, as already discussed. The higher the bandwidth values, the higher the number of WDM channels, resulting in a more flat-gain region in Er^{3+}-doped materials, making these materials suitable candidates for WDM and EDPWA applications, since they can operate not only in the C, but also in the S and L telecommunication bands.

The huge broadening observed in the emission spectra of Er^{3+} ion in orthorhombic Nb_2O_5 (84 nm) [21], even in a glass ceramic system, which is unusual, was higher than other Er^{3+}doped SiO_2-based host reported on literature, as $SiO_2–ZrO_2$, 24–28nm, [15], and $SiO_2–HfO_2$, 20–21 nm [9].

The most important effect caused by Yb^{3+} addition concerns the enhancement of the Er^{3+} emission, which clearly demonstrates an efficient energy transfer process from the Yb^{3+} to the Er^{3+} ions. Fig. 3(B) shows the comparison of sample S3 annealed at 900 °C doped only with Er^{3+} ions and co-doped with Er^{3+} and Yb^{3+} ions. An enhancement at 1.5 μm of almost one order of magnitude was observed for the co-doped sample S3, which contains orthorhombic Nb_2O_5. Besides, the NIR luminescence intensity drastically decreases for the samples containing the monoclinic phase, which has been seen more clearly by the lifetime measurements that will be discussed below.

Fig. 4(A)–(C) shows the photoluminescence (PL) decay curves for the Er^{3+}/Yb^{3+} $(1-x)SiO_2–xNb_2O_5$ nanocomposites for the annealing temperatures of 900, 1000 and 1100 °C respectively, and the $^4I_{13/2}$ lifetime values are given in Table 1. A non-exponential decay can be observed for all nanocomposites, consistent with the previous discussion about the presence of distinct symmetry sites occupied by Er^{3+} ions. The curves were fitted using a 2nd order exponential. The $\tau_{1/e}$ are also presented on the Table 1. The lifetimes decrease as the Nb_2O_5 content increases, in agreement with what is observed in the photoluminescence spectra, i.e., the Er^{3+} ions are occupying an Nb_2O_5-rich environment. The experimental lifetimes were lower than that exhibited for the Er^{3+}-doped $(1-x)SiO_2–xNb_2O_5$ nanocomposites [21], as well as the Er^{3+}/Yb^{3+} co-doped SiO_2 lifetimes, 10.6 ms [51]; Er^{3+} doped SiO_2, 12 ms [52] and comparable to Er^{3+}/Yb^{3+} co-doped pure Nb_2O_5 obtained in our laboratory, 1.6 ms (not reported here).

Also, it could be observed that increasing the annealing temperature resulted in shorter lifetimes, especially for samples S4 and S5. This observation can be explained by the Nb_2O_5 crystalline phase transformation, as observed by XRD and luminescence spectra. At higher temperature, densification is more pronounced and consequently can promote shorter distances between rare earth ions, enhancing energy migration processes, and therefore luminescence quenching, lowering the lifetime values.

3.1.3. Upconversion luminescence

Strong, visible with naked-eye UC luminescence was observed for the nanocomposites S2–S5 as shown in Fig. 5. Three emission bands were observed, with maxima at 525 nm, 545 nm (green emission) and 670 nm (red emission), which can be attributed to $^2H_{11/2}\rightarrow{}^4I_{15/2}$, $^4S_{3/2}\rightarrow{}^4I_{15/2}$ and $^4F_{9/2}\rightarrow{}^4I_{15/2}$ transitions, respectively. As discussed for the NIR emission in the present work and previous studies [21], the different Nb_2O_5 polymorphs with their different symmetries also affected the upconversion spectra. An inhomogeneous broadening was observed in all nanocomposites

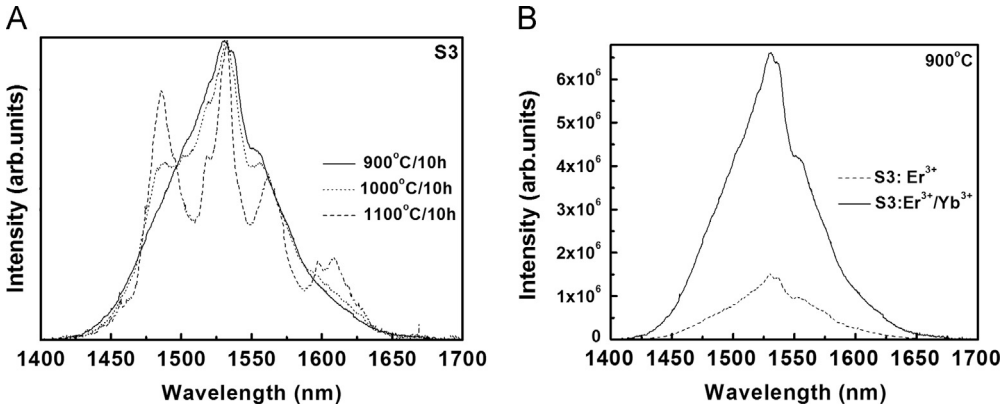

Fig. 3. (A) S3 spectra annealed at different temperatures (B) S3 NIR spectra comparison between 0.3 mol% Er^{3+}-doped and 0.3 mol% Er^{3+}/1.2 mol% Yb^{3+} co-doped nanocomposites.

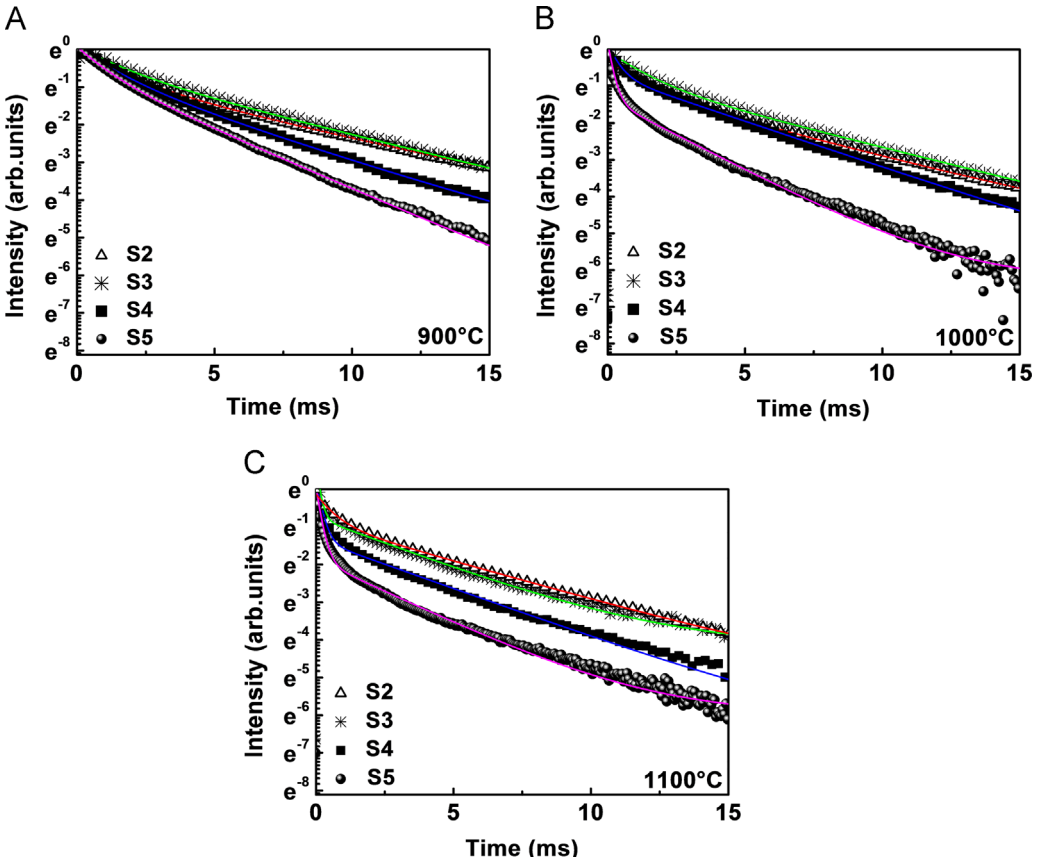

Fig. 4. PL decay curves for the $^4I_{13/2}$ level of Er^{3+} ions of 0.3 mol% Er^{3+}/1.2 mol% Yb^{3+} co-doped (1-*x*)SiO_2-*x*Nb_2O_5nanocomposites annealed at (A) 900 °C, (B) 1000 °C and (C) 1100 °C for 10 hrs.

containing the T phase, whereas, a lower FWHM values were observed when M-phase crystallizes, as it can be seen in Table 2.

Fig. 5A depicts the S2 spectra for different annealing temperatures. An increasing UC intensity was observed with increasing temperature from 900 to 1000 °C, and a decrease in intensity at 1100 °C. As observed in NIR emission, Er^{3+} luminescence from the ions occupying the Nb_2O_5 T-phase is much higher than that from the ions distributed in the M-phase. Accordingly, the luminescence intensity in the nanocomposite is directly related to the crystalline changes evidenced by X ray diffraction, i.e., the formation of T-phase at 900 and 1000 °C, with higher crystallinity and well-defined diffractions peaks at the latter temperature, and a mixture of T- and M-phases for the nanocomposite annealed at 1100 °C.

For S3 sample (Fig. 5B) we have observed that the higher intensity was obtained for the nanocomposite annealed at 900 °C and the intensity reduces at 1000 and 1100 °C. Although not observed in XRD analysis, this behavior could be explained by a T- and M-phases mixture, which would begin to take place even at 1000 °C. The indication of RE cluster formation, as discussed before, when Er^{3+} ions are distributed in the M-phase, results in energy migration between rare earth ions followed by luminescence quenching. This effect is clearly observed in samples S4 and S5 (Fig. 5C and D). More defined Stark's components of the multiplet are seen in the spectra for the nanocomposites annealed at 1000 and 1100 °C, which indicates that the Er^{3+} ions are occupying a lower number of distinct symmetry sites in the Nb_2O_5 crystalline phases, typical of Er^{3+} ions in M-phase. The different niobium content and annealing temperatures directly affect the upconversion intensity.

In order to elucidate UC mechanisms, spectra upon excitation at 980 nm with variable power between 35 and 170 mW were obtained. Fig. 6A shows the S3 nanocomposite spectra annealed at 900 °C which is representative of the behavior observed in all nanocomposites studied. Red emission was more intense than green one for the nanocomposites S2–S5. Figs. 6B–E present the emission intensity (I) as a function of pump power (P) (in a log–log graph) for nanocomposites S2–S5 annealed at 900 °C. Table 3 shows the results for nanocomposites S2–S5 annealed at 900, 1000 and 1100 °C showing *n* values around 2 for the green emission. With respect to the emission centered at 670 nm, a slope of 1.5 was observed in all samples.

A slope about 2 suggests two main possible mechanisms that have been extensively described in literature [29] for both green and red UC emissions: Excited State Absorption (ESA) and Energy Transfer Upconversion (ETU), which are schematically represented on Fig. 7A. In the framework of the ESA mechanism, the Er^{3+} ions are excited to the $^4I_{11/2}$ level by ground state absorption (GSA) of the 980 nm pump, where a second photon of same energy is absorbed to bring the excited ion to the $^4F_{7/2}$ level, which then decay non-radiatively to $^4H_{11/2}$ and $^4S_{3/2}$, and emit at 545 and 525 nm, respectively, corresponding to the $^2H_{11/2} \rightarrow {}^4I_{15/2}$, $^4S_{3/2} \rightarrow {}^4I_{15/2}$ transitions in the green. The excited ions in $^2H_{11/2}$ and $^4S_{3/2}$ levels can also decay non-radiatively to $^4F_{9/2}$ and emit in the red (at 670 nm) through the $^4F_{9/2} \rightarrow {}^4I_{15/2}$ transition. The contribution of this mechanism can be considered low since in the samples containing only Er^{3+} ions (0.3 mol% Er^{3+}, not reported here) there is no significant upconversion. In the ETU mechanism, there are two possible situations. In the first one, two Er^{3+} ions in the excited state $^4I_{11/2}$ by GSA can exchange energy and while one of them is excited to $^4F_{7/2}$ level, the other decays to ground state. In the other situation one Yb^{3+} ion is excited to $^2F_{5/2}$ and one Er^{3+} ion is excited to $^4I_{11/2}$ by GSA, then the Yb^{3+} ion transfers energy to the Er^{3+} ion which is excited to $^4F_{7/2}$ level. In both cases, the Er^{3+} ions excited in the $^4F_{7/2}$ level decay non-radiatively to $^4H_{11/2}$

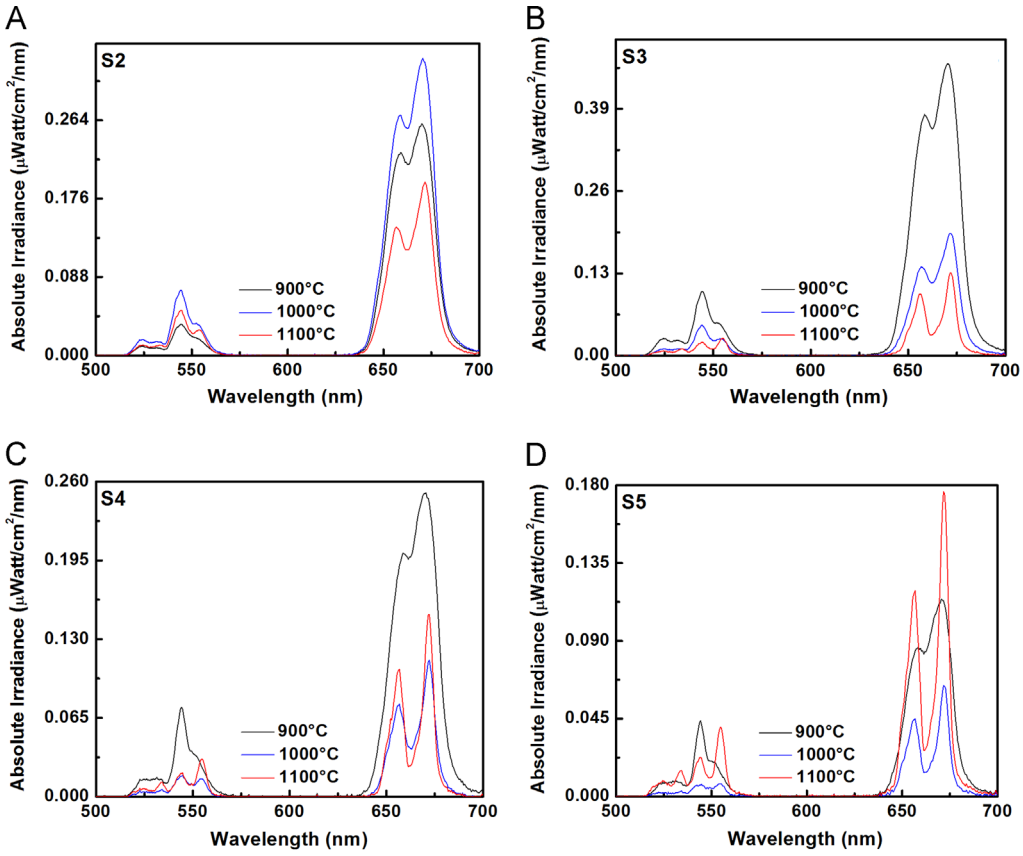

Fig. 5. Upconversion emission spectra of the Er^{3+} ions of 0.3 mol% Er^{3+}/1.2 mol% Yb^{3+} co-doped (1-*x*)SiO_2-*x*Nb_2O_5 nanocomposites annealed at 900 °C, 1000 °C and 1100 °C for 10 hrs: (A) S2, (B) S3, (C) S4 and (D) S5 upon excitation at 980 nm.

Table 2
FWHM values at 675 and 670 nm comparision for Er^{3+}/Yb^{3+} co-doped $(1-x)SiO_2$–xNb_2O_5 nanocomposites S2, S3, S4 and S5 annealed at 900 °C, 1000 °C and 1100 °C.

Nanocomposites (°C)	FWHM at 657 nm (nm)	FWHM at 670 nm (nm)
S2 – 900	12	15
S2 – 1000	12	15
S2 – 1100	12	15
S3 – 900	11	15
S3 – 1000	11	15
S3 – 1100	8	7
S4 – 900	10	16
S4 – 1000	11	9
S4 – 1100	8	9
S5 – 900	10	16
S5 – 1000	9	7
S5 – 1100	8	6

and $^4S_{3/2}$, (with subsequent emission from this state in the green) and further decay to $^4F_{9/2,}$ and emit in the red. The Er^{3+} ion excited to the $^4I_{11/2}$ level by ground state absorption (GSA) can also decay non-radiatively to $^4I_{13/2}$ followed by absorption of a second photon bringing the excited ion to the $^4F_{9/2}$ level, with subsequent $^4F_{9/2}$ to $^4I_{15/2}$ transition. As the Yb^{3+} ions are essential for obtaining high upconversion intensity, the latter mechanism has been considered the most significant one in this work.

Regarding the emission centered at 670 nm, a slope parameter *n* lower than two has already been observed in other Er^{3+} doped glasses [46] and can be explained by another process involving energy transfer and cross-relaxation (Fig. 7B). This possible mechanism consists of three absorbed photons giving two emitted photons (*n* of 1.5). First, one Er^{3+} ion is excited to the $^4F_{7/2}$ state through ESA or ETU process (where two infrared photons populates the $^4F_{7/2}$ state), and one photon is absorbed by another Er^{3+} ion, populating the $^4I_{11/2}$ excited state. After a cross-relaxation process, both Er^{3+} ions relax to the excited $^4F_{9/2}$ state [46], with subsequent red emission from this state to the ground state.

3.2. Planar waveguides

3.2.1. Optical characterization

Table 4 brings together the optical parameters of Er^{3+}/Yb^{3+} co-doped planar waveguides W1–W5. Crack-free waveguides were obtained for all Si/Nb ratios. An increase of the refractive index values with increasing Nb content was observed and the values are in agreement with that calculated by the Lorentz–Lorenz equation [20], indicating that a full densification was achieved, except for the sample W1, which still contains pores. The densification is crucial to avoid porosity and consequently the presence of water molecules and OH groups inside the pores. A complete elimination of OH from the porous and host has been successfully achieved for the samples W2–W5. Longer annealing at 900 °C has been used to eliminate OH groups remaining in sample W1, which impact the NIR luminescence as will be described in the following.

To ensure that all films have a homogeneous densification at any depth, their refractive index profile has been analyzed, as depicted in Fig. 8. The refractive index profile were reconstructed from the effective indexes at 632.8 nm by an inverse Wentzel-Kramers-Brillouin method [53]. The uniform distribution of the refractive indexes across the thickness shows the high homogeneity of the waveguides and the small difference between TE and TM modes indicates a low birefringence. The refractive index value added to the homogeneous distribution attested the achievement of full densification, avoiding the presence of OH

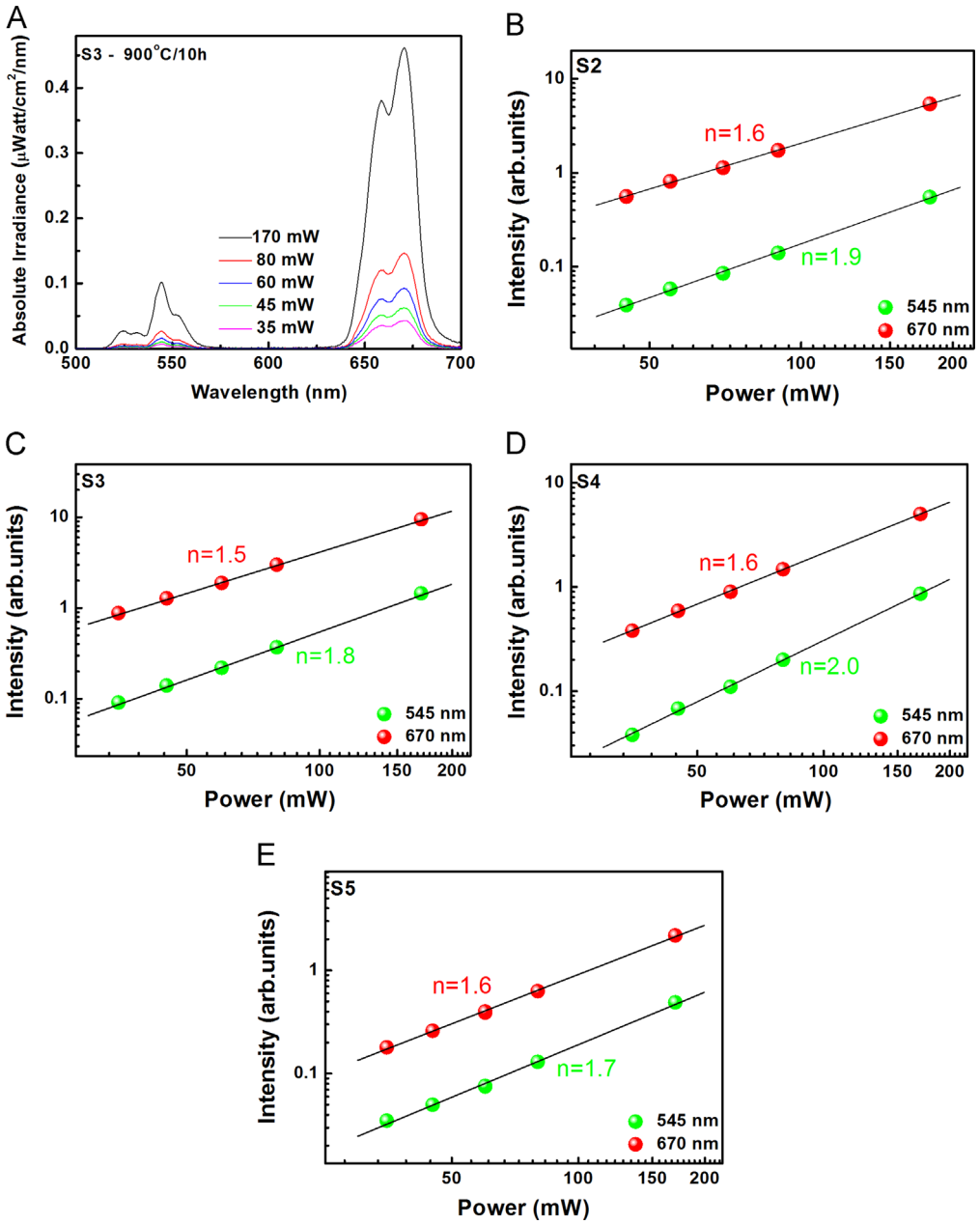

Fig. 6. (A) Upconversion emission spectra of the Er^{3+} ions of 0.3 mol% Er^{3+}/1.2 mol% Yb^{3+} co-doped S3 nanocomposite annealed at 900 °C with excitation power from 35 to 170 mW. Log–log plots of upconversion intensity at 545 and 670 nm as function of excitation power for (B) S2, (C) S3, (D) S4, (E) S5 0.3 mol% Er^{3+}/1.2 mol% Yb^{3+} co-doped (1-*x*)SiO_2-*x*Nb_2O_5 nanocomposites annealed at 900 °C for 10 hrs.

Table 3
Photons number (*n*) calculated by the power law $I \alpha P^n$ for the 0.3 mol% Er^{3+}/1.2 mol% Yb^{3+} co-doped (1-*x*)SiO_2-*x*Nb_2O_5nanocomposites at different annealing temperatures.

Samples (°C)	n at 545 nm	n at 670 nm
S2 – 900	1.9	1.6
S2 – 1000	2.0	1.5
S2 – 1100	2.1	1.5
S3 – 900	1.8	1.5
S3 – 1000	1.7	1.5
S3 – 1100	1.7	1.5
S4 – 900	2.0	1.6
S4 – 1000	2.0	1.6
S4 – 1100	1.8	1.4
S5 – 900	1.7	1.6
S5 –1000	1.9	1.6
S5 –1100	1.7	1.3

groups, which represents one of the most important contributions to luminescence quenching in sol–gel derived materials, through multiphonon relaxation.

3.2.2. NIR luminescence

The PL emission spectra of the Er^{3+}/Yb^{3+} co-doped waveguides W2–W5 are outlined in Fig. 9A (without further annealing) and 9B (annealed at 900ºC for different times). A broad band emission was observed for all waveguides with maxima at 1531 nm with a shoulder at 1560 nm, characteristic of $^4I_{13/2} \rightarrow {}^4I_{15/2}$ transition of Er^{3+} ions. The 1.5 μm emission was observed for all samples except W1, which probably still presented OH groups. The number of Stark components augmented with increasing Nb content demonstrating, as observed for the nanocomposites, that Er^{3+} and Yb^{3+} ions are occupying Nb_2O_5-rich sites. After a long

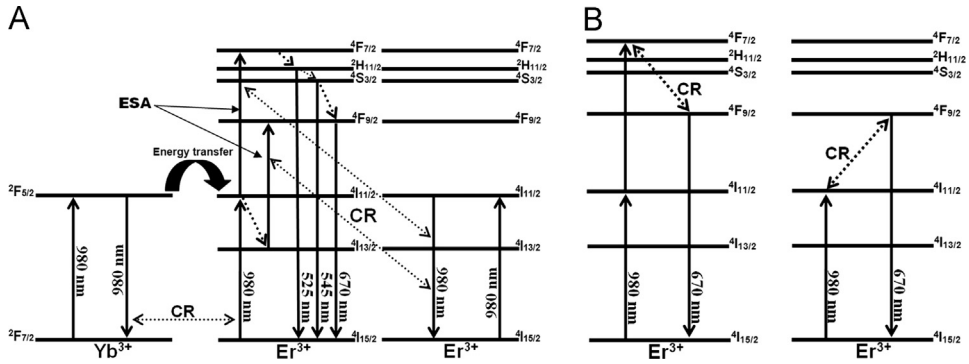

Fig. 7. Upconversion mechanisms showing the Er^{3+} and Yb^{3+} transitions involved: (A) ESA and ETU, (C) $n=1.5$ photons.

Table 4
Optical parameters for the 0.3 mol%/1.2 mol% Yb^{3+} co-doped (1-x)SiO_2-xNb_2O_5 waveguides W1, W2, W3, W4, and W5.

Waveguides Parameters	W1 (TE/TM)	W2 (TE/TM)	W3 (TE/TM)	W4 (TE/TM)	W5 (TE/TM)
Number of modes at 632.8 nm	2/2	3/3	4/4	6/6	6/6
Refractive index at 632.8 nm	1.5038/ 1.5021	1.6046/ 1.6048	1.6850/ 1.6882	1.7764/ 1.7794	1.8620/ 1.8604
Number of modes at 1538 nm	1/1	1/1	2/2	2/2	2/2
Refractive index at 1538 nm	1.4865/ 1.4869	1.5807/ 1.5816	1.6545/ 1.6569	1.7384/ 1.7408	1.8090/ 1.8126
Film thickness (μm)	1.50	1.54	1.64	1.70	1.70

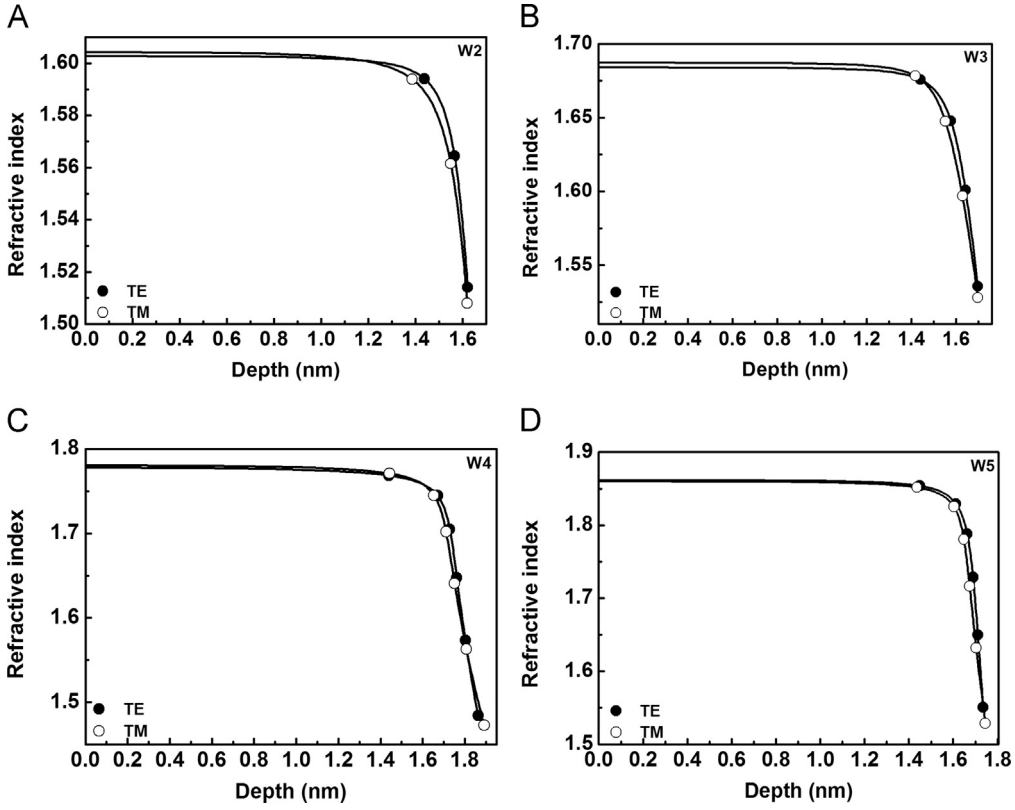

Fig. 8. Refractive index profiles of the 0.3 mol% Er^{3+}/1.2 mol% Yb^{3+} co-doped planar waveguides W2, W3, W4, and W5, reconstructed from modal measurements at 632.8 nm for TE and TM polarization. The effective refractive indices of the TE (•) and TM (○) modes are reported.

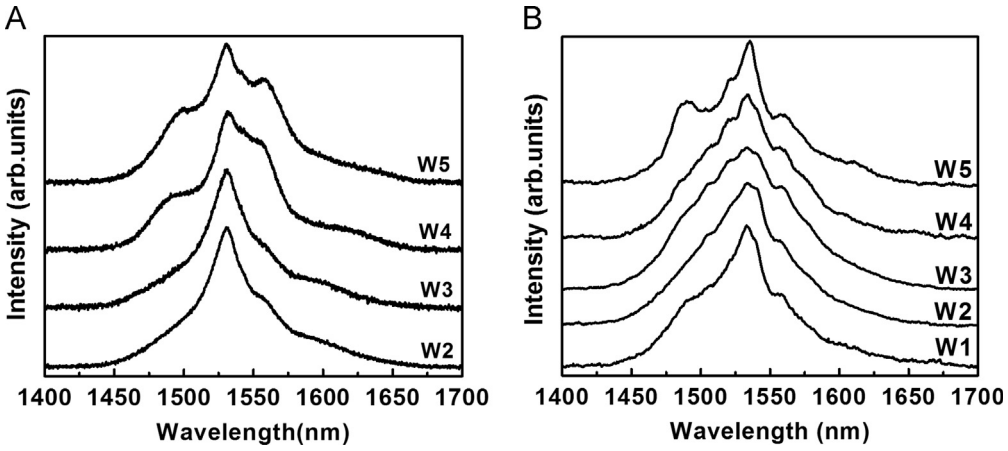

Fig. 9. (A) NIR photoluminescence spectra relative to the $^4I_{13/2} \rightarrow {}^4I_{15/2}$ transition of the Er^{3+} ions of 0.3 mol% Er^{3+}/1.2 mol% Yb^{3+} co-doped planar waveguides W2–W5 without further annealing; (B) NIR photoluminescence spectra relative to the $^4I_{13/2} \rightarrow {}^4I_{15/2}$ transition of the Er^{3+} ions of 0.3 mol% Er^{3+}/1.2 mol% Yb^{3+} co-doped planar waveguides W1–W5 after a long time of annealing at 900 °C;

Table 5
Full width at half-maximum (FWHM) and $^4I_{13/2}$ excited level lifetimes of the Er^{3+} ions for waveguides 0.3 mol% Er^{3+}/ 1.2 mol% Yb^{3+} co-doped $(1-x)SiO_2$–xNb_2O_5 waveguides W1–W5. (A) without posterior annealing, (B) after long time of annealing.

Waveguides	Main emission peak (nm) (B)	FWHM (nm) (A)	FWHM (nm) (B)/ time of annealing (hours)	$^4I_{13/2}$ excited level lifetime (ms) $\tau_{1/e}$ (A)
W1	1533	–	62/109	
W2	1533	44	69/87	5.4
W3	1533	40	88/87	5.2
W4	1533	54	70/8.5	5.2
W5	1535	78	65/8.5	4.6

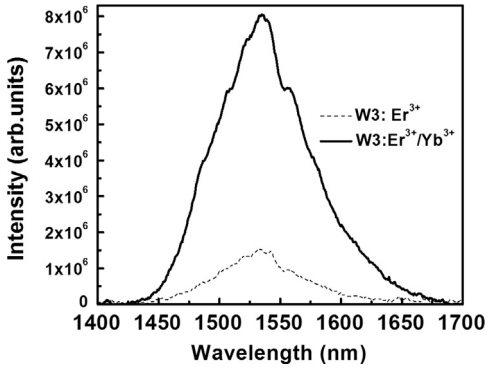

Fig. 10. W3 NIR spectra comparison between 0.3 mol% Er^{3+}-doped and 0.3 mol% Er^{3+}/1.2 mol% Yb^{3+} co-doped planar waveguides.

time of annealing the remnant OH groups were eliminated, resulting in NIR emission for this waveguide, as shown in Fig. 9B.

The bandwidths, measured by the FWHM values, are shown in Table 5. Large FWHM were obtained for all waveguides even without a long time of annealing, with values which increased with increasing Nb_2O_5 content, from 44 to 78 nm. After a long time of annealing, it could be observed an increase of the FWHM values for waveguides W1–W3, achieving 88nm for the last one, and a decrease for W4 and W5, i.e., increasing the Nb content. This behavior could be explained by the fact that after a long time of annealing for W4 and W5, which have 40 and 50 mol% of Nb, Nb_2O_5 crystalline phase transition could take place, which can change the symmetry sites occupied by the rare earth ions resulting in increasing FWHM values for W1–W3 waveguides (T-phase) and decreasing FWHM values for W4 and W5

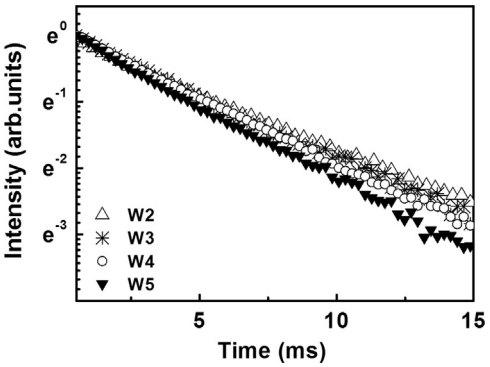

Fig. 11. PL decay curves for the $^4I_{13/2}$ level of Er^{3+} ions of 0.3 mol% Er^{3+}/1.2 mol% Yb^{3+} co-doped waveguides W2–W5 without further annealing.

(T+M-phases) corroborating with the nanocomposites XRD analysis discussed previously. The FWHM values obtained in the present work are much larger than in other SiO_2-based waveguides as discussed before. Comparing with our previous work [21], Yb^{3+} ions promote not only a broadening of luminescence but also an enhancement in intensity, denoting an efficient energy transfer to the Er^{3+} ions (Fig. 10), particularly in the T-phase, making the W2 and W3 promising waveguides for photonic applications regarding optical amplifiers in the S, C and L-telecommunication band. Fig. 11 shows the PL decay curves for the planar waveguides without further annealing, and the $^4I_{13/2}$ lifetime values are given in Table 5. The $^4I_{13/2}$ lifetime change from 5.4 to 4.6 ms as the niobium content increases.

3.2.3. Upconversion luminescence

Figs. 12A–D depicts the upconversion emission spectra for the waveguides W2 to W5, respectively. Green (525 and 545 nm) and red (670 nm) emissions were observed for the waveguides which can be attributed to $^2H_{11/2} \rightarrow {}^4I_{15/2}$, $^4S_{3/2} \rightarrow {}^4I_{15/2}$ and $^4F_{9/2} \rightarrow {}^4I_{15/2}$ transitions, respectively. Although the measurements were performed in the reflection configuration instead of the coupled mode (waveguiding configuration), an intense and visible to the naked eye UC emission of the planar waveguides was observed under excitation at 980 nm. Normally to obtain high UC luminescence from waveguides, the measurements should be performed exciting the waveguiding TE_0 mode and detecting the scattered light from the surface of the waveguides [46,47].

The green and red emission UC may take place via excited state absorption (ESA), and energy transfer upconversion (ETU) mechanisms, as described before and summarized in the schematic diagram

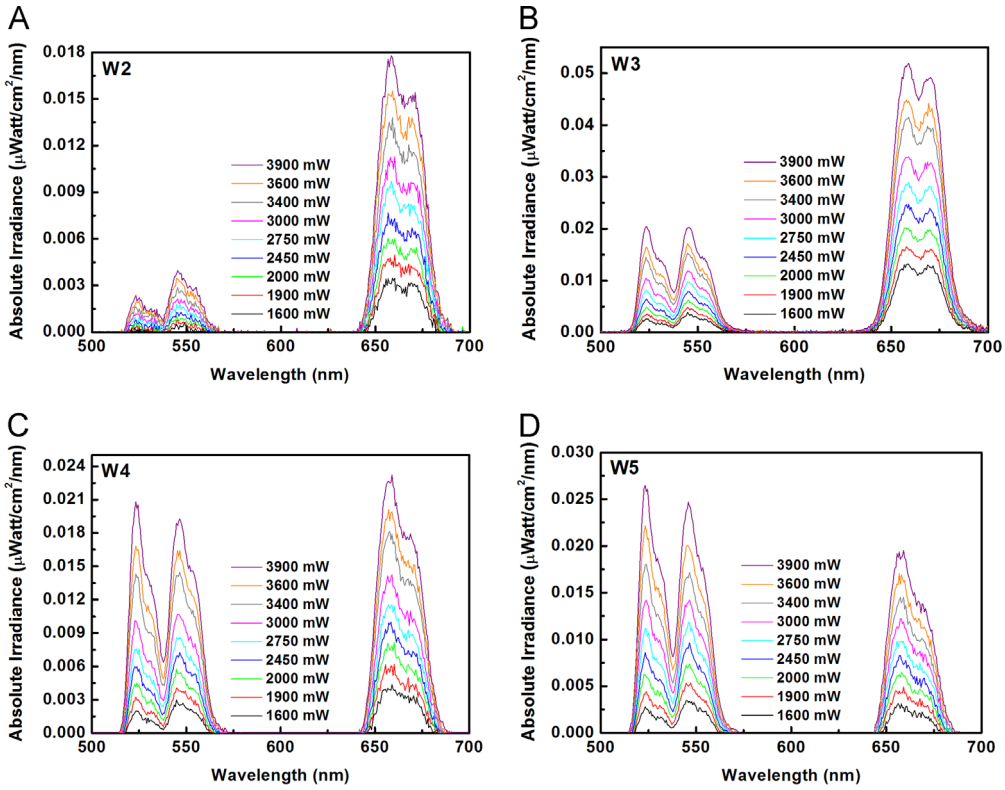

Fig. 12. Upconversion emission spectra of the Er^{3+} ions of 0.3 mol% Er^{3+}/1.2 mol% Yb^{3+} co-doped planar waveguides with excitation power from 1600 to 3900 mW (A) W2, (B) W3, (C) W4, and (D) W5.

in Fig. 7. For the planar waveguides, as a high excitation power was used, another mechanism that can take place is the two photon absorption (TPA) [45,54], which can be achieved by the simultaneous two photons absorption involving real or virtual levels. The latter mechanism becomes more noticeable when high excitation power is used. In this work, as Er^{3+} ions are used, the TPA process after excitation at 980 nm populates the $^4F_{7/2}$ efficiently (real level), resulting in highly efficient green emission. This mechanism can explain the high intensity in the green emission in the case of planar waveguides in comparison with nanocomposites. In addition, it may be observed that the green emission is more intense when the samples are excited under higher power.

For the nanocomposites, a low power regime was considered, and the UC emission intensity increased with distinct power dependence for green and red emissions indicating that different mechanisms may contribute to both UC emissions. As the rate constants of the $^4S_{3/2}$ and $^4F_{9/2}$ levels are not the same, the high power limit is also not identical for both states. Consequently, in an intermediate power regime (as in the case of planar waveguide), the populations of the $^4S_{3/2}$ and $^4F_{9/2}$ levels will show different power dependences and hence the emission effective color can be tuned with the laser power as demonstrated in Fig. 8.

The green and red intensity ratio also changes with the composition. As the niobium content increases, the contribution of non-radiative processes diminishes. Consequently, the non-radiative decay from $^4S_{3/2}$ to $^4F_{9/2}$ is reduced, and the green emission is favored.

Fig. 13 shows the CIE chromaticity diagram, in which color coordinates were calculated based on the UC emission spectra for the respective waveguides. It can be observed that the color depends on the excitation power and Nb content. Especially for the waveguides W2 and W3, color can be tuned by the excitation power used. The tunable upconversion observed for the waveguides W2 and W3 suggests that this materials have potential applications as visible range lasers, energy converters and other photonic applications.

4. Conclusions

The effect of Yb^{3+} addition on structural and its correlation with luminescent properties of sol–gel Er^{3+} doped SiO_2–Nb_2O_5 nanocomposites and planar waveguides have been reported. In comparison with previous work [20], the higher amount of rare earth in the samples favored the T-phase crystallization at lower temperatures (900 °C), influencing the Nb_2O_5 nucleation and crystallization process, as well as stabilizing the T-phase at higher temperatures, since only partial phase transformation to the M-phase occurs at 1100 °C. The structural change, caused by Ln^{3+} ions concentration increase (by Yb^{3+} addition), results in strong effects on the NIR luminescence of Er^{3+} and NIR-to-visible UC emission. Enhanced and broadband NIR luminescence was observed with FWHM values ranging from 59 to 89 nm and $^4I_{13/2}$ lifetime values of milliseconds, which change as a function of niobium content and thermal annealing. The different Nb_2O_5 polymorphs affected the photophysical features, with higher intensity and longer lifetimes for the nanocomposite and planar waveguides annealed at 900 °C, which contains only the T-phase. The Yb^{3+} co-doping enhanced the luminescence intensity in comparison with single Er^{3+}-doped $(1-x)SiO_2$–xNb_2O_5 of our previous work, indicating an efficient energy transfer between $^2F_{5/2} \rightarrow {}^2F_{7/2}$ and the $^4I_{15/2} \rightarrow {}^4I_{11/2}$ transitions of Yb^{3+} and Er^{3+} ions, respectively.

Enhanced intensity and broadband emission in homogeneous and fully densified crack-free planar waveguides were prepared. These features make the waveguides W2 and W3 promising materials for integrated optics applications, more specifically EDWA and WDM devices.

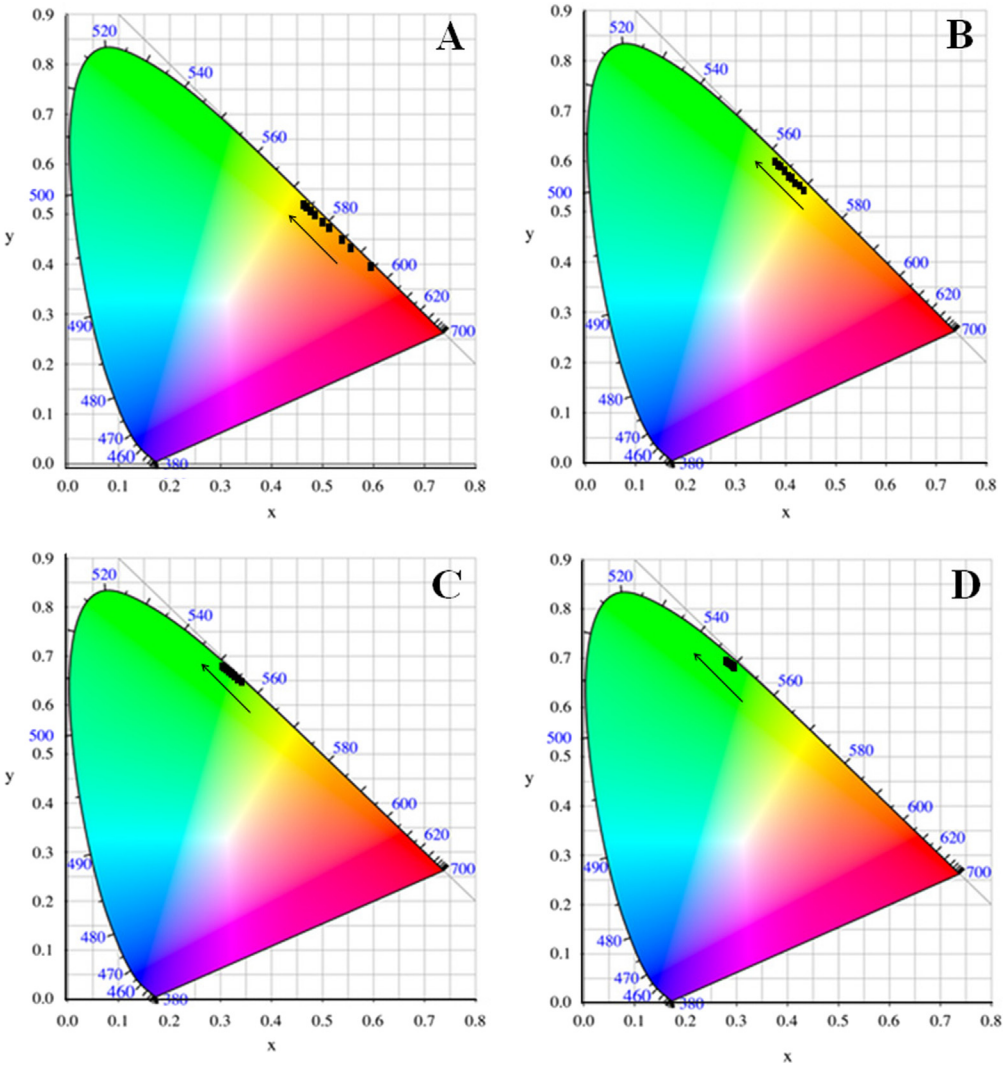

Fig. 13. 1931 CIE chromaticity diagram coordinates of 0.3 mol% Er^{3+}/1.2 mol% Yb^{3+} co-doped planar waveguides with excitation power from 1600 to 3900 mW.

Strong, visible to the naked-eye, UC emission bands assigned to the $^2H_{11/2} \rightarrow {}^4I_{15/2}$, $^4S_{3/2} \rightarrow {}^4I_{15/2}$ and $^4F_{9/2} \rightarrow {}^4I_{15/2}$ transitions from Er^{3+} ions were observed under excitation at 980 nm, at room temperature. The observed green and red UC emissions in nanocomposites and planar waveguides reported in this work may take place via ESA and ETU. A strong contribution of Yb^{3+} to UC intensity was observed.

Multicolor tunability of enhanced UC emission in planar waveguides was observed as a function of the laser power source and composition. The planar waveguides possess optical qualities that make them promising candidates for shorter wavelength laser sources, energy converters devices and other photonic applications.

Acknowledgments

The authors would like to thank FAPESP, CAPES, and CNPq for financial support and Alexandre Thomaz Aquino for Figures edition.

References

[1] M. Ferrari, G. Righini, Rare-earth-doped glasses for integrated optical amplifiers, in: N.S. Hussain, J.D.S. Santos (Eds.), Physics and Chemistry of Rare-Earth Ions Doped Glasses, Trans Tech Publishers, Switzerland, 2008, p. 300.

[2] A.J. Kenyon, Recent developments in rare-earth doped materials for optoelectronics, Prog. Quantum Electron. 26 (2002) 225–284.

[3] P. Goldner, A. Ferrier, O. Guilhot Noël, Rare earth-doped crystals for quantum information processing, in: G. Bünzli Jean-Claude, V.K. Pecharsky (Eds.), Handbook on the Physics and Chemistry of Rare Earths, Elsevier, Oxford, 2015 1-78.

[4] A. Polman, F.C.J.M. van Veggel, Broadband sensitizers for erbium-doped planar optical amplifiers: review, J. Opt. Soc. Am. B 21 (2004) 871–892.

[5] A. Polman, Erbium as a probe of everything? Phys. B: Condens. Matter 300 (2001) 78–90.

[6] J.L. Ferrari, K.O. Lima, L.J.Q. Maia, S.J.L. Ribeiro, A.S.L. Gomes, R.R. Gonçalves, Broadband NIR emission in sol–gel Er^{3+}-activated $SiO_2Ta_2O_5$ glass ceramic planar and channel waveguides for optical application, J. Nanosci. Nanotechnol. 11 (2011) 2540–2544.

[7] R.M. Almeida, A.C. Marques, R. Cabeça, L. Zampedri, A. Chiasera, M. Ferrari, Photoluminescence of erbium-doped silicate sol–gel planar waveguides, J. Sol–Gel Sci. Technol. 31 (2004) 317–322.

[8] L. Zampedri, M. Ferrari, C. Armellini, F. Visintainer, C. Tosello, S. Ronchin, R. Rolli, M. Montagna, A. Chiasera, S. Pelli, G.C. Righini, A. Monteil, C. Duverger, R.R. Gonçalves, Erbium-activated silica–titania planar waveguides, J. Sol–Gel Sci. Technol. 26 (2003) 1033–1036.

[9] S. Berneschi, A. Chiappini, M. Ferrari, S. Pelli, G.C. Righini, Erbium doped silica-hafnia glass ceramic waveguides, Phys. Status Solidi (c) 8 (2011) 2875–2879.

[10] Y. Jestin, C. Armellini, A. Chiappini, A. Chiasera, M. Ferrari, C. Goyes, M. Montagna, E. Moser, G. Nunzi Conti, S. Pelli, R. Retoux, G.C. Righini, G. Speranza, Erbium activated HfO_2 based glass–ceramics waveguides for photonics, J. Non-Cryst. Solids 353 (2007) 494–497.

[11] F.A. Sigoli, R.R. Gonçalves, A.S.S. de Camargo, L.A.O. Nunes, Y. Messaddeq, S.J.L. Ribeiro, Preparation and characterization of erbium and ytterbium co-doped sol–gel SiO_2:HfO_2 films for planar waveguides, Opt. Mater. 30 (2007) 600–607.

[12] F.A. Sigoli, R.R. Gonçalves, Y. Messaddeq, S.J.L. Ribeiro, Erbium- and ytterbium-doped sol–gel SiO_2–HfO_2 crack-free thick films onto silica on silicon substrate, J. Non-Cryst. Solids 352 (2006) 3463–3468.

[13] R.R. Gonçalves, G. Carturan, M. Montagna, M. Ferrari, L. Zampedri, S. Pelli, G.C. Righini, S.J.L. Ribeiro, Y. Messaddeq, Erbium-activated HfO_2-based waveguides for photonics, Opt. Mater. 25 (2004) 131–139.

[14] R.R. Gonçalves, G. Carturan, L. Zampedri, M. Ferrari, M. Montagna, A. Chiasera, G.C. Righini, S. Pelli, S.J.L. Ribeiro, Y. Messaddeq, Sol–gel Er-doped SiO_2–HfO_2 planar waveguides: a viable system for 1.5 mm application, Appl. Phys. Lett. 81 (2002) 28–30.

[15] Cd.S. Cunha, J.L. Ferrari, D.C. de Oliveira, L.J.Q. Maia, A.S.L. Gomes, S.J.L. Ribeiro, R.R. Gonçalves, NIR luminescent Er^{3+}/Yb^{3+} co-doped SiO_2–ZrO_2 nanostructured planar and channel waveguides: optical and structural properties, Mater. Chem. Phys. 136 (2012) 120–129.

[16] C. Goyes, M. Ferrari, C. Armellini, A. Chiasera, Y. Jestin, G.C. Righini, F. Fonthal, E. Solarte, CO_2 laser annealing on erbium-activated glass–ceramic waveguides for photonics, Opt. Mater. 31 (2009) 1310–1314.

[17] R.R. Gonçalves, J.J. Guimarães, J.L. Ferrari, L.J.Q. Maia, S.J.L. Ribeiro, Active planar waveguides based on sol–gel Er^{3+}-doped SiO_2–ZrO_2 for photonic applications: morphological, structural and optical properties, J. Non-Cryst. Solids 354 (2008) 4846–4851.

[18] R.R. Gonçalves, Y. Messaddeq, A. Chiasera, Y. Jestin, M. Ferrari, S.J.L. Ribeiro, Erbium-activated silica–zirconia planar waveguides prepared by sol–gel route, Thin Solid Films 516 (2008) 3094–3097.

[19] J.L. Ferrari, K.O. Lima, L.J.Q. Maia, R.R. Gonçalves, Sol–gel preparation of near-infrared broadband emitting Er^{3+}-doped SiO_2–Ta_2O_5 nanocomposite films, Thin Solid Films 519 (2010) 1319–1324.

[20] F.T. Aquino, J.L. Ferrari, S.J.L. Ribeiro, A. Ferrier, P. Goldner, R.R. Gonçalves, Broadband NIR emission in novel sol–gel Er^{3+}-doped SiO_2–Nb_2O_5 glass ceramic planar waveguides for photonic applications, Opt. Mater. 35 (2013) 387–396.

[21] F.T. Aquino, R.R. Pereira, J.L. Ferrari, S.J.L. Ribeiro, A. Ferrier, P. Goldner, R.R. Gonçalves, Unusual broadening of the NIR luminescence of Er^{3+}-doped Nb_2O_5 nanocrystals embedded in silica host: preparation and their structural and spectroscopic study for photonics applications, Mater. Chem. Phys. 147 (2014) 751–760.

[22] I. Nowak, M. Ziolek, Niobium compounds: preparation, characterization, and application in heterogeneous catalysis, Chem. Rev. 99 (1999) 3603–3624.

[23] M.A. Aegerter, Sol–gel niobium pentoxide: a promising material for electrochromic coatings, batteries, nanocrystalline solar cells and catalysis, Sol. Energy Mater. Sol. Cells 68 (2001) 401–422.

[24] L. Petit, T. Cardinal, J.J. Videau, E. Durand, L. Canioni, M. Martines, Y. Guyot, G. Boulon, Effect of niobium oxide introduction on erbium luminescence in borophosphate glasses, Opt. Mater. 28 (2006) 172–180.

[25] A. Jha, B. Richards, G. Jose, T. Teddy-Fernandez, P. Joshi, X. Jiang, J. Lousteau, Rare-earth ion doped TeO_2 and GeO_2 glasses as laser materials, Prog. Mater. Sci. 57 (2012) 1426–1491.

[26] D. Manzani, J.L. Ferrari, F.C. Polachini, Y. Messaddeq, S.J.L. Ribeiro, 1.5 [small mu]m and visible up-conversion emissions in Er^{3+}/Yb^{3+} co-doped tellurite glasses and optical fibers for photonic applications, J. Mater. Chem. 22 (2012) 16540–16545.

[27] M.P. Hehlen, N.J. Cockroft, T.R. Gosnell, A.J. Bruce, Spectroscopic properties of Er^{3+}- and Yb^{3+}-doped soda-lime silicate and aluminosilicate glasses, Phys. Rev. B 56 (1997) 9302–9318.

[28] F. Auzel, Compteur quantique par transfert d'energie entre de Yb^{3+} a Tm^{3+} dans uns tungstate mixte et dans verre germanate, C. R. Acad. Sci. Paris 263 (1966) 819–821.

[29] F. Auzel, Upconversion and anti-stokes processes with f and d ions in solids, Chem. Rev. 104 (2004) 139–174.

[30] O. Toma, S. Georgescu, Competition between green and infrared emission in Er:$YLiF_4$ upconversion lasers, Opt. Commun. 284 (2011) 388–397.

[31] F. Lahoz, C. Pérez-Rodríguez, S.E. Hernández, I.R. Martín, V. Lavín, U.R. Rodríguez-Mendoza, Upconversion mechanisms in rare-earth doped glasses to improve the efficiency of silicon solar cells, Sol. Energy Mater. Sol. Cells 95 (2011) 1671–1677.

[32] S. Ivanova, F. Pellé, Strong 1.53 μm to NIR–VIS–UV upconversion in Er-doped fluoride glass for high-efficiency solar cells, J. Opt. Soc. Am. B 26 (2009) 1930–1938.

[33] B.M. van der Ende, L. Aarts, A. Meijerink, Lanthanide ions as spectral converters for solar cells, Phys. Chem. Chem. Phys. 11 (2009) 11081–11095.

[34] G.S. Maciel, A. Biswas, R. Kapoor, P.N. Prasad, Blue cooperative upconversion in Yb^{3+}-doped multicomponent sol–gel-processed silica glass for three-dimensional display, Appl. Phys. Lett. 76 (2000) 1978–1980.

[35] M. Haase, H. Schäfer, Upconverting nanoparticles, Angew. Chem. Int. Ed. 50 (2011) 5808–5829.

[36] N. Bogdan, F. Vetrone, G.A. Ozin, J.A. Capobianco, Synthesis of ligand-free colloidally stable water dispersible brightly luminescent lanthanide-doped upconverting nanoparticles, Nano Lett. 11 (2011) 835–840.

[37] F. Vetrone, R. Naccache, V. Mahalingam, C.G. Morgan, J.A. Capobianco, The active-core/active-shell approach: a strategy to enhance the upconversion luminescence in lanthanide-doped nanoparticles, Adv. Funct. Mater. 19 (2009) 2924–2929.

[38] V.D. Rodríguez, V.K. Tikhomirov, J. Méndez-Ramos, A.C. Yanes, V.V. Moshchalkov, Towards broad range and highly efficient down-conversion of solar spectrum by Er^{3+}–Yb^{3+} co-doped nano-structured glass-ceramics, Sol. Energy Mater. Sol. Cells 94 (2010) 1612–1617.

[39] R. Lisiecki, E. Augustyn, W. Ryba-Romanowski, M. Żelechower, Er-doped and Er, Yb co-doped oxyfluoride glasses and glass–ceramics, structural and optical properties, Opt. Mater. 33 (2011) 1630–1637.

[40] H. Gong, L. Lin, X. Zhao, E.Y.B. Pun, D.L. Yang, H. Lin, Mixing up-conversion excitation behaviors in Er^{3+}/Yb^{3+}-codoped aluminum germanate glasses for visible waveguide devices, J. Alloy Compd. 503 (2010) 133–137.

[41] F.A. Bomfim, J.R. Martinelli, L.R.P. Kassab, N.U. Wetter, J.J. Neto, Effect of the ytterbium concentration on the upconversion luminescence of Yb^{3+}/Er^{3+} co-doped PbO–GeO_2–Ga_2O_3 glasses, J. Non-Cryst. Solids 354 (2008) 4755–4759.

[42] M.A. Forastiere, G.C. Righini, M. Brenci, S. Pelli, M. Ferraris, D. Milanese, Modelling of diffractive structures in photorefractive Er/Yb–co-doped glass waveguides, Opt. Lasers Eng. 39 (2003) 333–344.

[43] U.R. Rodríguez-Mendoza, E.A. Lalla, J.M. Cáceres, F. Rivera-López, S.F. León-Luís, V. Lavín, Optical characterization, 1.5 μm emission and IR-to-visible energy upconversion in Er^{3+}-doped fluorotellurite glasses, J. Lumin. 131 (2011) 1239–1248.

[44] D. Mohanty, V. Rai, Y. Dwivedi, S. Rai, Enhancement of upconversion intensity in Er^{3+} doped tellurite glass in presence of Yb^{3+}, Appl. Phys. B: Lasers Opt. 104 (2011) 233–236.

[45] J.L. Ferrari, K. de Oliveira Lima, E. Pecoraro, R.A.S. Ferreira, L.D. Carlos, R.R. Gonçalves, Color tunability of intense upconversion emission from Er^{3+}-Yb^{3+} co-doped SiO_2–Ta_2O_5 glass ceramic planar waveguides, J. Mater. Chem. 22 (2012) 9901–9908.

[46] R.R. Gonçalves, G. Carturan, L. Zampedri, M. Ferrari, A. Chiasera, M. Montagna, G.C. Righini, S. Pelli, S.J.L. Ribeiro, Y. Messaddeq, Infrared-to-visible CW frequency upconversion in erbium activated Silica–Hafnia waveguides prepared by sol–gel route, J. Non-Cryst. Solids 322 (2003) 306–310.

[47] A. Polman, Erbium implanted thin film photonic materials, J. Appl. Phys. 82 (1997) 1–39.

[48] S.F.H. Correia, V. de Zea Bermudez, S.J.L. Ribeiro, P.S. Andre, R.A.S. Ferreira, L.D. Carlos, Luminescent solar concentrators: challenges for lanthanide-based organic–inorganic hybrid materials, J. Mater. Chem. A 2 (2014) 5580–5596.

[49] E.I. Ko, J.G. Weissman, Structures of niobium pentoxide and their implications on chemical behavior, Catal. Today 8 (1990) 27–36.

[50] C. Duverger, M. Montagna, R. Rolli, S. Ronchin, L. Zampedri, M. Fossi, S. Pelli, G.C. Righini, A. Monteil, C. Armellini, M. Ferrari, Erbium-activated silica xerogels: spectroscopic and optical properties, J. Non-Cryst. Solids 280 (2001) 261–268.

[51] P.M. Peters, D.S. Funk, A.P. Peskin, D.L. Veasey, N.A. Sanford, S.N. Houde-Walter, J.S. Hayden, Ion-exchanged waveguide lasers in Er^{3+}/Yb^{3+} codoped silicate glass, Appl. Opt. 38 (1999) 6879–6886.

[52] L.H. Slooff, M.J.A. de Dood, A. van Blaaderen, A. Polman, Effects of heat treatment and concentration on the luminescence properties of erbium-doped silica sol–gel films, J. Non-Cryst. Solids 296 (2001) 158–164.

[53] K. Chiang, Construction of refractive-index profiles of planar dielectric waveguides from the distribution of effective indexes, J. Lightwave Technol. 3 (1985) 385–391.

[54] G.A. Kumar, M. Pokhrel, A. Martinez, R.C. Dennis, I.L. Villegas, D.K. Sardar, Synthesis and spectroscopy of color tunable Y_2O_2S:Yb^{3+},Er^{3+} phosphors with intense emission, J. Alloy. Compd. 513 (2012) 559–565.